

ARTICLE

Reduction-Induced CO Dissociation by a $[\text{Mn}(\text{bpy})(\text{CO})_4][\text{SbF}_6]$ Complex and its Relevance in Electrocatalytic CO_2 Reduction

Received 00th January 20xx,
Accepted 00th January 20xx

DOI: 10.1039/x0xx00000x

Hsin-Ya Kuo^{a,†}, Steven E. Tignor^{a,†}, Tia S. Lee^a, Danrui Ni^a, James Eujin Park^a, Gregory D. Scholes^a, and Andrew B. Bocarsly^{a*}

$[\text{Mn}(\text{bpy})(\text{CO})_3\text{Br}]$ is recognized as a benchmark electrocatalyst for CO_2 reduction to CO, with the doubly reduced $[\text{Mn}(\text{bpy})(\text{CO})_3]^-$ proposed to be the active species in the catalytic mechanism. The reaction of this intermediate with CO_2 and two protons is expected to produce the tetracarbonyl cation, $[\text{Mn}(\text{bpy})(\text{CO})_4]^+$, thereby closing the catalytic cycle. However, this species has not been experimentally observed. In this study, $[\text{Mn}(\text{bpy})(\text{CO})_4][\text{SbF}_6]$ (**1**) was directly synthesized and found to be an efficient electrocatalyst for the reduction of CO_2 to CO in the presence of H_2O . Complex **1** was characterized using X-ray crystallography as well as IR and UV-Vis spectroscopy. The redox activity of **1** was determined using cyclic voltammetry and compared with that of benchmark manganese complexes, e.g., $[\text{Mn}(\text{bpy})(\text{CO})_3\text{Br}]$ (**2**) and $[\text{Mn}(\text{bpy})(\text{CO})_3(\text{MeCN})][\text{PF}_6]$ (**3**). Infrared spectroscopic analyses indicated that CO dissociation occurs after a single-electron reduction of complex **1**, producing a $[\text{Mn}(\text{bpy})(\text{CO})_3(\text{MeCN})]^-$ species. Complex **1** was experimentally verified as both a precatalyst and an on-cycle intermediate in homogeneous Mn-based electrocatalytic CO_2 reduction.

Introduction

CO_2 reductions are thermodynamically uphill¹ and mechanistically complex, involving multiple proton-coupled electron transfer (PCET) processes,² and hence require efficient catalysts.³ Among the various suitable methods, electrochemical CO_2 reduction utilizing transition metal complexes has attracted much attention^{3–10} due to the ease of tunability both at the metal and ligand sites.¹¹ Moreover, many molecular electrocatalysts are capable of reducing CO_2 to CO, which can be further transformed into hydrocarbons via Fischer–Tropsch synthesis.¹²

In molecular CO_2 -reduction electrocatalysts, the polypyridine ligand not only stabilizes the reduced metal center but also functions as a redox-active site via the conjugated π system, thereby enabling the multiple electron transfer steps necessary for CO_2 transformation.³ Recently, owing to the high cost and low abundance of second- and third-row transition metals, focus has shifted towards first-row transition metals.⁸ For example, the electrocatalytic activity of $[\text{Mn}(\text{bpy})(\text{CO})_3\text{Br}]$ for CO_2 reduction was first reported by Bourrez *et al.* in 2011.¹⁰ The use of weak Brønsted acids was necessary for this Mn electrocatalyst to be active towards CO_2 reduction.^{10,13}

The proposed mechanism, shown in Figure 1 is favored based on experimental observations^{14,15} and theoretical investigations.^{16,17}

The active catalyst, $[\text{Mn}(\text{bpy})(\text{CO})_3]^-$ (red box, Figure 1), generated by two one-electron reductions of $[\text{Mn}(\text{bpy})(\text{CO})_3\text{Br}]$ along with Br^- loss, has an open coordination site. Binding of CO_2 to the open

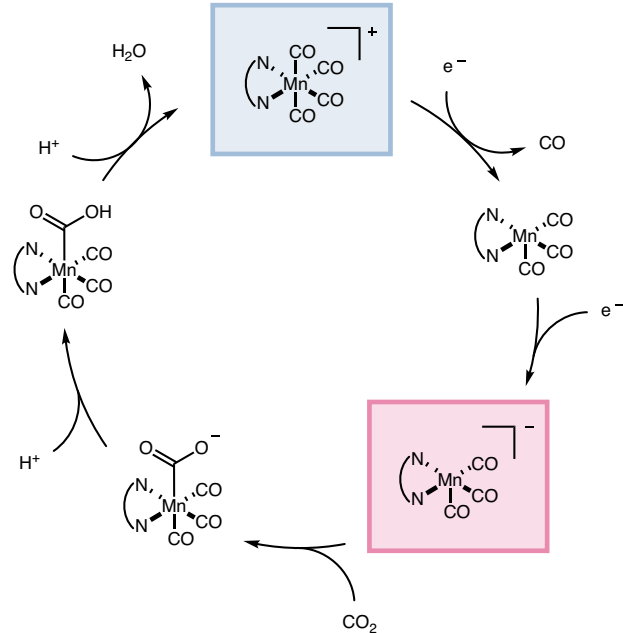


Figure 1. Proposed mechanism for CO_2 reduction to CO by $[\text{Mn}(\text{bpy})(\text{CO})_4]^+$ (blue box) by way of the active species $[\text{Mn}(\text{bpy})(\text{CO})_3]^-$ (red box) in the presence of weak Brønsted acids.

^a Department of Chemistry, Princeton University, Princeton, New Jersey 08544, United States.

† These authors contributed equally to this work.

Electronic Supplementary Information (ESI) available: [details of any supplementary information available should be included here]. See DOI: 10.1039/x0xx00000x

coordination site is followed by protonation to yield $[\text{Mn}(\text{bpy})(\text{CO})_3(\text{CO}_2\text{H})]$. A final protonation followed by H_2O loss generates $[\text{Mn}(\text{bpy})(\text{CO})_4]^+$ (blue box, Figure 1), which then

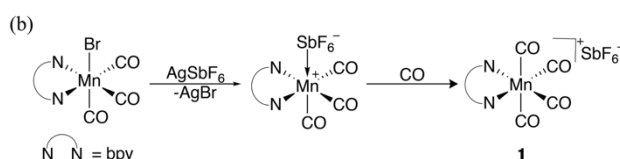
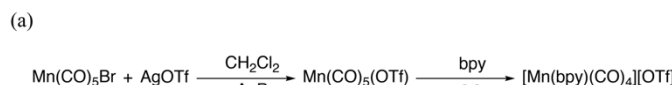
undergoes a one-electron reduction, CO liberation, and a second electron reduction to regenerate the active catalyst. The tetracarbonyl cation however, has not been experimentally verified as an intermediate in the Mn-based catalytic cycle, although it seems chemically reasonable to suggest its presence.¹⁸ Demonstration of the existence and reaction chemistry of the key $[\text{Mn}(\text{bpy})(\text{CO})_4]^+$ intermediate is thus central to confirming the proposed mechanism.

Herein, we present the synthesis and characterization of the tetracarbonyl complex $[\text{Mn}(\text{bpy})(\text{CO})_4]\text{SbF}_6$ (**1**). We compare its electrochemical properties with those of two benchmark catalysts, $[\text{Mn}(\text{bpy})(\text{CO})_3\text{Br}]$ (**2**) and $[\text{Mn}(\text{bpy})(\text{CO})_3(\text{MeCN})]\text{PF}_6$ (**3**), and study its role in the mechanism for CO_2 reduction using electrochemistry, FT-IR, and UV-Vis spectroelectrochemistry.

Results and Discussion

Synthesis and Characterization

Based on the reported synthesis of $[\text{Re}(\text{bpy})(\text{CO})_4]^+$,^{18,19} the preparation of **1** was expected to proceed via the metathesis of $\text{Mn}(\text{CO})_5\text{Br}$ with silver triflate (AgOTf) in CH_2Cl_2 (Scheme 1a), followed by the addition of bpy to produce the desired product. However, this synthetic approach generated an intractable mixture. Unlike the stable $\text{Re}(\text{CO})_5(\text{OTf})$,¹⁹ this undesirable result may be attributed to the sensitivity of $\text{Mn}(\text{CO})_5(\text{OTf})$ to light and moisture, which caused partial decomposition to yield $\text{Mn}_2(\text{CO})_{10}$,²⁰ making the ligation of bpy impossible.



Scheme 1. (a) Proposed synthesis of tetracarbonyl cation via $\text{Mn}(\text{CO})_5(\text{OTf})$. (b) Formation of **1** via Lewis acid-base reaction with CO.

An alternative approach was carried out by treating **2** with AgSbF_6 in CH_2Cl_2 under continuous purging with CO,²¹ to yield the desired complex as a SbF_6^- salt. Compared to the condition without added CO, the continuous CO purging significantly inhibited side reactions, and a moderate yield of **1** was obtained (40%) after 30 min. As shown in Scheme 1b, the formation of **1** likely involves the generation of the Lewis acid-base adduct $[\text{Mn}(\text{bpy})(\text{CO})_3(\text{SbF}_6)]$, followed by CO substitution.^{21,22} This intermediate seems to be relatively unstable due to the weakly coordinating SbF_6^- anion, and thus it should be noted that the purity of **1** is sensitive to the reaction time. After a prolonged reaction time (4 h), we found byproducts that could not be effectively separated via purification. Complex **1** was characterized using UV-Vis, NMR, and FT-IR spectroscopies, as well as X-ray crystallography.

Complexes **1-3** are presented in Figure 2a, and the UV-Vis absorbance spectrum in MeCN (Figure 2b) shows a broad peak in the near-UV-visible range corresponding to a metal-to-ligand charge

transfer (MLCT) absorption, i.e., $\text{Mn}(\text{I}) \rightarrow \text{bpy}(\pi^*)$. Consistent with the spectrochemical series, complex **1**, bearing two carbonyl ligands in the axial position, displays the most blue-shifted MLCT band at ~330 nm, whereas complexes **2** and **3**, with axial ligation of bromide and MeCN, exhibit MLCT bands at 416 and 369 nm, respectively. This effect of axial ligand substitution on the MLCT shift is consistent with those of other reported Mn-carbonyl pyridyl-carbene-based complexes.²³ The axial ligands (CO, Br, and MeCN) all exhibit σ -type interaction between the metal d_{z^2} orbital and the ligand orbitals. Furthermore, CO and Br also participate via π -type interactions: CO can accept metal electron density into its empty π^* orbital through back-bond donation, yielding a large HOMO-LUMO gap, whereas Br can donate electron density to the metal d-orbital, resulting in a small HOMO-LUMO gap. On the other hand, MeCN can bind to the metal center only via a σ -type interaction, as it has no symmetry-allowed orbitals for the aforementioned π bonding.

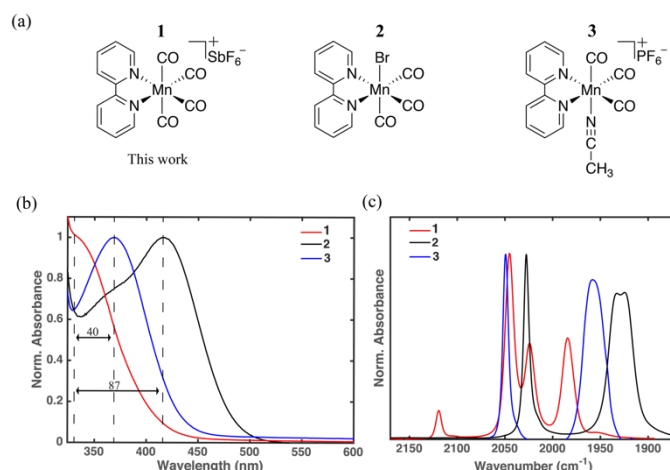


Figure 2. (a) Representation of the synthesized complexes **1-3**. (b) UV-Vis absorption spectra in MeCN at 298 K at 1 cm path length with MLCT band positions shown. CO- and MeCN-ligated complexes **1** and **3** display a higher-energy MLCT band compared to Br-ligated **2**. (c) FT-IR spectra are evident in the FT-IR spectra.

The FT-IR spectra of the three complexes in MeCN are shown in Figure 2c, and the solid-state ATR-IR spectra are included in Figure S1^t. Both complexes **2** and **3** exhibit a typical three-peak profile between 1900 and 2100 cm^{-1} , which is consistent with the facial arrangement of tricarbonyl metal complexes. The two bands at the lower frequency correspond to symmetric and antisymmetric stretching of the two equatorial COs (trans to the bpy), whereas the remaining band at the highest frequency results from the stretching mode of the axial CO,^{24,25} which is trans to the other axial ligand (i.e., CO, Br, or MeCN). Furthermore, the CO stretching modes of **2** are all at frequencies lower than those of **3**; this shift is consistent with an increase in the π^* donation to the carbon of the axial CO in the presence of the π -donor (i.e., Br), and in agreement with the observed MLCT band shift. Complex **1** has C_{2v} symmetry, and is expected to exhibit four IR active carbonyl stretching bands.²⁶ Analogous to a reported Re complex,¹⁹ these four bands were assigned as an A_1 mode (2130 cm^{-1}), a B_1 mode (2046 cm^{-1}), another A_1 mode (2024 cm^{-1}), and a B_2 mode (1984 cm^{-1}). One striking feature in the IR spectrum of **1** (Fig. 2c) is that one of the A_1 bands appears at

an unexpectedly high frequency (2130 cm^{-1}). This indicates a significant decrease in the π -back bond donation between the Mn center and one or more of the CO ligands, and this frequency is near the value for free CO in a heptane solution (2140 cm^{-1}).²¹ While it is not surprising that π -back bonding effects were diminished in the trans-CO geometry, the shift of one CO stretching frequency so far upfield was unexpected.

We performed density functional theory (DFT) calculations at the M06 level of theory to study the vibrational modes of interest in complex **1**. The vibrational spectrum was computed at the optimized geometry, and the simulated vibrational spectrum is in agreement with the experimental data (Figure S2[†]). Four intense CO stretching bands were calculated (unscaled) at 2210 , 2119 , 2109 , and 2072 cm^{-1} . The displacement vectors of the carbonyl vibration modes are included in Figure S3[†]. The mode calculated at 2210 cm^{-1} (i.e., the highest CO stretching frequency) shows that all the four CO ligands move in phase (i.e., symmetric stretching) and one of the axial CO ligands exhibits an amplitude slightly different from that of the others. In accord with the experimental data, this suggests that the large shift of the highest stretching frequency (experimentally found to be 2130 cm^{-1}) can be explained by a group stretching vibration of all the four carbonyl ligands. The second-highest stretching frequency at 2119 cm^{-1} is assigned to the two axial COs moving out of phase, i.e., asymmetric stretching. The remaining two modes at 2109 and 2072 cm^{-1} correspond to the symmetric and asymmetric stretching of the two equatorial CO ligands, respectively.

Complex **1** was recrystallized by vapor diffusion of hexane into a concentrated dichloromethane solution. Single crystal X-ray diffraction analysis of the sample yielded the structure shown in Figure 3; the selected bond lengths and angles are listed in Table 1. The $\text{C}_{11}\text{-Mn-C}_{14}$ angle (177.01°) is similar to those of reported bpy-ligated Re tetracarbonyl analogs,^{18,27} ranging from 177 – 179° . This bond angle is in agreement with a DFT-calculated value of 177.93° and indicates that the level of theory applied is suitable for describing the current system. An interesting feature of **1** is the significant difference between the two axial CO bond lengths ($\sim 0.02\text{ \AA}$), which has also been observed for other Re¹⁸ and Mn²⁸ tetracarbonyl analogs.

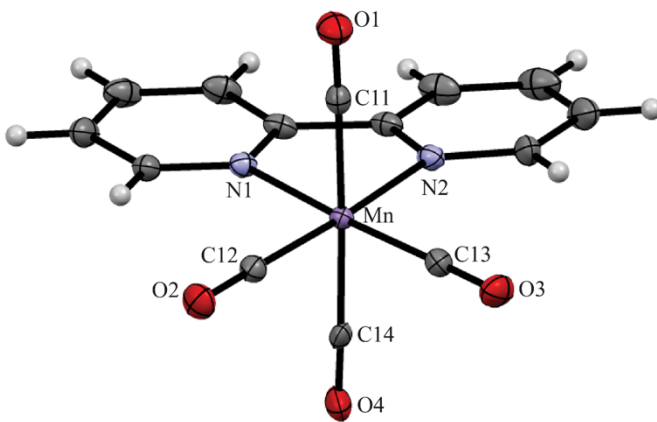


Figure 3. Molecular structure of **1** with selected atom labeling and thermal ellipsoids shown at 50% probability. Counter anion and solvent molecules have been omitted for clarity.

Table 1. Selected Bond Lengths (\AA) and Angles ($^\circ$) for **1**.

Mn-C11	1.879(3)
Mn-C12	1.825(3)
Mn-C13	1.837(3)
Mn-C14	1.915(3)
Mn-N1	2.048(3)
Mn-N2	2.044(3)
C11-O1	1.114(5)
C12-O2	1.141(5)
C13-O3	1.135(5)
C14-O4	1.098(5)
N1-Mn-N2	79.0(1)
N1-Mn-C12	95.9(1)
N2-Mn-C13	95.9(1)
C12-Mn-C13	89.2(1)
C11-Mn-C14	177.0(1)

As expected, the two axial Mn-CO bonds show a pronounced difference (1.879 \AA vs 1.915 \AA); both are longer than the bonds of the two equatorial CO ligands, which are trans to the bpy. This observation is attributed to reduced Mn \rightarrow CO π -back bonding due to the presence of a strong π acceptor, as evidenced by the FT-IR data. This description is further substantiated by the significantly shorter $\text{C}_{14}\text{-O}_4$ bond (1.098 \AA).

Electrochemistry

The redox processes of the three complexes under Ar were analyzed using cyclic voltammetry (CV) in MeCN with 0.1 M tetrabutylammonium hexafluorophosphate (TBAH). At a scan rate of 250 mV/s (Figure 4a), complex **1** displays two reductive waves at -1.48 and -1.86 V vs Fc/Fc^+ ; the two reductive peaks do not exhibit return waves over the scan rates ranging from 25 to 1000 mV/s (Fig. S4[†]). This lack of reversibility suggests that chemical reactions occur after each reduction, as discussed later. Moreover, a comparison between complex **1** and the reported $[\text{Re}(\text{bpy})(\text{CO})_4][\text{OTf}]$ reveals interesting similarities and differences.¹⁹ The first reduction processes occur at potentials ca. 100 mV more positive than those of their neutral precursors, i.e., complex **2** or $[\text{Re}(\text{bpy})(\text{CO})_3(\text{Cl})]$. However, the first reductive wave of the Re analog remains quasi-reversible, whereas that of **1** is not reversible, which suggests a possible ligand loss.

The CV curve of **1** under Ar is overlaid on those of **2** and **3** in Figure 4b. The first reduction peaks of **1** and **3** are similar, and they both appear at more positive potentials ($\sim 140\text{ mV}$) than that of **2**. The first reduction seems relatively sensitive to the replacement of the axial bromide with neutral ligands. Furthermore, the lack of reversibility of the first reduction process for these three complexes (i.e., no return wave) suggests a chemical reaction following the first reduction. Analogous to the Re tetracarbonyl species,¹⁸ for which the first reduction is assigned as bpy-based, we propose that the first reduction of **1** is also into the bpy π^* orbital, followed by an internal charge transfer to move the electron into a metal centered d-

orbital.²⁹ An electrochemically induced CO dissociation from the singly reduced $[\text{Mn}(\text{bpy})(\text{CO})_4]^0$ can be hypothesized to account for this cyclic voltammetric response, which has also been reported for the Re analog. Such reduction-induced CO dissociation was also observed in other systems, including our recently reported CN-bridged Mn complex³⁰ and other tetracarbonyl analogs containing group 6 metals.^{31,32} The subsequent reductions for these three complexes occur at almost identical potentials, and thus suggest similar reductive processes. In line with the literature,^{10,13,17,33} Br-ligated **2** readily undergoes Br^- loss followed by dimerization after the first reduction, due to the transient nature of the 16-electron radical $[\text{Mn}(\text{bpy})(\text{CO})_3]$ at room temperature.³⁴ The similar redox processes of complexes **1** and **2** suggest that the second reduction process of **1** is the reduction of $[\text{Mn}_2(\text{CO})_6(\text{bpy})_2]$ followed by the formation of $[\text{Mn}(\text{bpy})(\text{CO})_3]^-$ via dimer cleavage as is discussed in the section on spectroscopic studies.

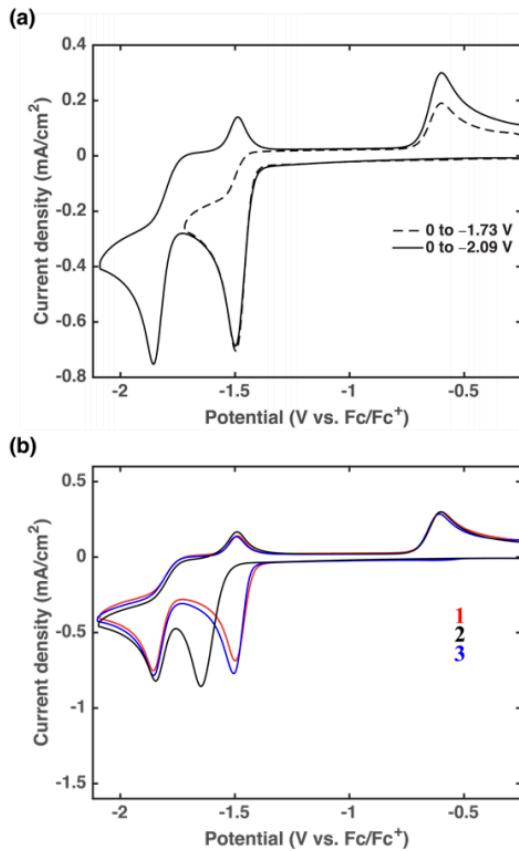


Figure 4. (a) CV data of **1** (1 mM) at two different switching potentials. The data were recorded at 250 mV/s under Ar in 0.1 M TBAH in MeCN with a 3-mm-diameter glassy carbon working electrode, a platinum foil counter electrode, and a Ag/Ag^+ nonaqueous reference electrode. All the potentials are referenced to Fc/Fc^+ . (b) CV data comparison for the three complexes under study. The other conditions were similar to those shown in panel a.

In the reverse scan, complex **1** shows two oxidative waves at -1.50 and -0.60 V vs Fc/Fc^+ ; the more cathodic peak only appears after the second reduction potential is reached (Figure 4a). The two oxidative waves overlap with those of **2** and **3**, as shown in Figure 4b. The more negative peak is assigned to the oxidation of $[\text{Mn}(\text{bpy})(\text{CO})_3]^-$, which leads to dimer formation. The more positive peak is associated with the oxidation of the Mn–Mn-bonded dimer. In addition, in the second reductive scan shown in (Figure S5[†]), the

first reductive peak of **1** is initiated at a potential slightly more positive than that observed during the first scan; this new potential is consistent with the first reductive onset current of **3**. This observation suggests the possibility of CO dissociation during the first reduction process of **1** and the subsequent formation of the MeCN-coordinated species. The new peak is also apparent in the second scan of **2** (Figure S5[†]), which corresponds to the formation of **3** and is in good agreement with the literature.¹⁰

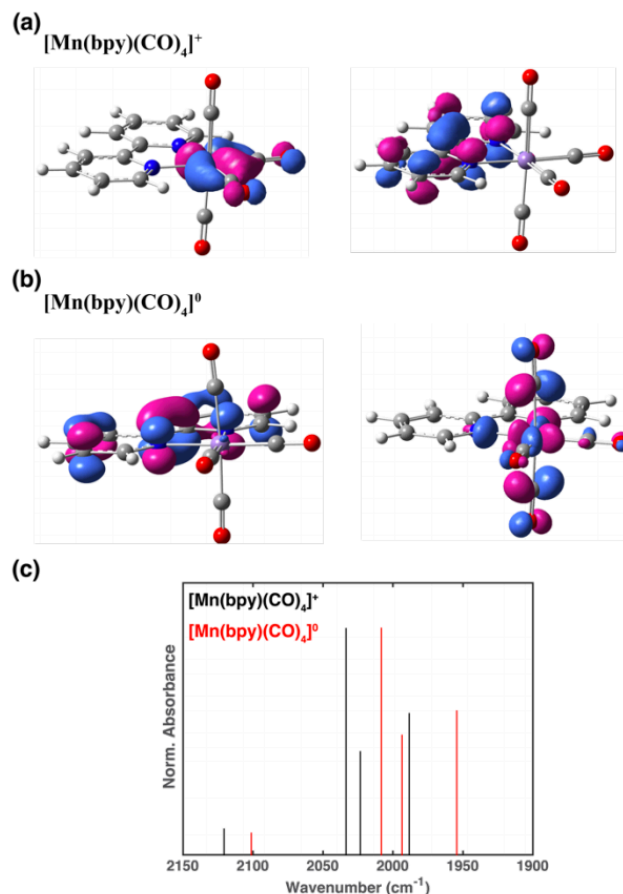


Figure 5. (a) HOMO (left) and LUMO (right) of $[\text{Mn}(\text{bpy})(\text{CO})_4]^+$. (b) SOMO (left) and LUMO (right) of $[\text{Mn}(\text{bpy})(\text{CO})_4]^0$. (c) Calculated carbonyl stretching frequencies.

To gain insight into the species formed upon the one-electron reduction of **1**, we compared the DFT calculations of $[\text{Mn}(\text{bpy})(\text{CO})_4]^+$ and $[\text{Mn}(\text{bpy})(\text{CO})_4]^0$ at the M06 level of theory. The optimized geometry structure was obtained using the crystal structure of **1** as the initial input. The calculated lowest unoccupied molecular orbital (LUMO) of $[\text{Mn}(\text{bpy})(\text{CO})_4]^+$ is localized on the bpy, while the highest occupied molecular orbital (HOMO) is delocalized over the Mn center and the two equatorial COs (Figure 5a), which is in agreement with the Mn–CO back-bonding evidenced by the experimental data. In comparison, the electronic structure of the singly reduced $[\text{Mn}(\text{bpy})(\text{CO})_4]^0$ species reveals differences (Figure 5b); the LUMO is delocalized over the Mn center and π^* orbitals of the two axial CO ligands, whereas the extra electron of the singly occupied molecular orbital resides in the π^* orbitals of bpy. Due to orbital overlap, this results in additional electron density on the Mn center and increased π back-bonding into the π^* (CO) antibonding orbitals, resulting in a weakening of the CO bonds.¹⁴ In Figure 5c, the calculated vibration

line spectra show that the reduced species $[\text{Mn}(\text{bpy})(\text{CO})_4]^0$ exhibits red shifted $\nu(\text{CO})$ frequencies relative to the nonreduced counterpart. However, one of the axial CO ligands exhibits relatively decreased π back-bonding. These results suggest the weakening of the metal carbonyl bond interaction in $[\text{Mn}(\text{bpy})(\text{CO})_4]^0$, thereby leading to the CO dissociation following one-electron reduction of the initial cationic complex.

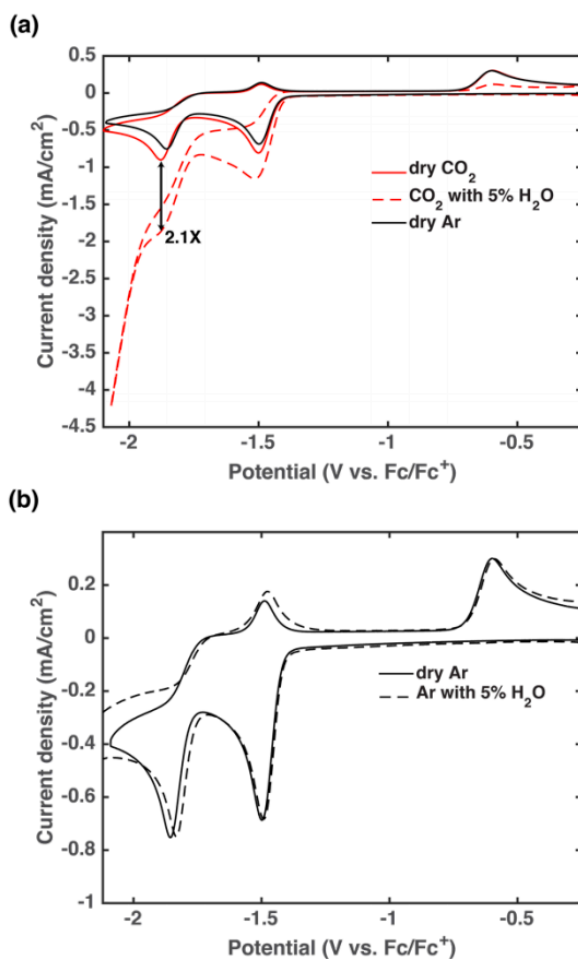


Figure 6. CV data of **1** with and without 5% H_2O under CO_2 (a) and Ar (b) at 250 mV/s. All the other conditions were similar to those given in Figure 4.

To investigate the activity of **1** in the presence of CO_2 with and without water, we studied the electrochemistry of **1** under dry and wet CO_2 , as shown in Figure 6a. Under dry CO_2 conditions (red solid line), slight current increases were observed at both reduction potentials. Upon addition of H_2O (5%, red dashed line), a significant current enhancement (2.1 times) occurs at the second reduction potential, and the oxidative waves at -1.50 and -0.60 V vs Fc/Fc^+ are diminished; both phenomena indicate that CO_2 reduction is catalyzed by the species associated with the second reduction potential of **1**. Additionally, upon addition of water under CO_2 , the shape of the first reduction wave changes with a slight current increase, whereas no significant change occurs for the wet electrolyte under Ar, as shown in Figure 6b. The effect of the H_2O content on the catalytic activity was surveyed by monitoring the current at -1.88 V vs Fc/Fc^+ (Fig. S6^t). Increasing the H_2O amount from 5% to 7% (v/v) did not result in a higher current at the second reduction peak, indicating that at 5% water, the proton demand was saturated.³⁵ Thus, complex **1** was

experimentally demonstrated to be electrochemically active in the presence of CO_2 and H_2O .

To probe this electrochemical reaction, a bulk electrolysis with 25 μmol complex **1** (1 mM) was carried out at -1.88 V vs Fc/Fc^+ in the wet electrolyte under CO_2 . Carbon monoxide was identified as the reaction product, and was monitored and quantified through headspace analysis using gas chromatography (GC). The product analysis in Figure S7a^t shows that the amount of CO is directly proportional to the charge passed, with an average Faradaic efficiency (ϕ_{CO}) of $80 \pm 4.0\%$ for CO production over a 3 h observation period. The remaining charge was balanced H_2 production directly from the electrode surface. No soluble organic products, including formate, were found using ^1H NMR of the post-electrolysis electrolyte (Figure S8^t). This result not only verifies the electrochemical activity of **1** under CO_2 but also suggests that complex **1** is highly selective for CO production. Furthermore, CO was also observed when a bulk electrolysis with **1** (1 mM) was conducted at -1.48 V vs Fc/Fc^+ (the first- reduction peak potential) under otherwise identical conditions. The CO evolution data for both potentials are compared in Figure S7b^t. We noted that the CO

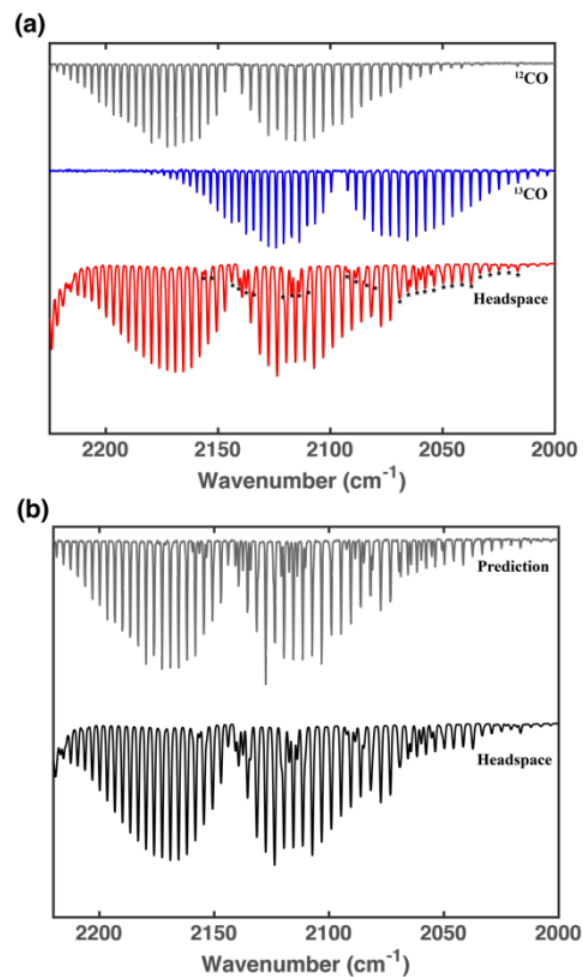


Figure 7. (a) Analysis of the headspace with FT-IR following a 3 h electrolysis of **1** with $^{13}\text{CO}_2$ at -1.86 V vs. Fc/Fc^+ in 0.1 M TBAH in MeCN with 5% H_2O . The presence of ^{13}CO (*) confirms the electrocatalytic CO_2 conversion to CO. (b) A plot of the headspace (black trace) is compared with a predicted spectrum with 30% ^{13}CO and 70% ^{12}CO (grey trace).

evolution at the first reduction potential (-1.48 V vs Fc/Fc⁺) reached a plateau after ~2 h; this observation can be attributed to the saturation of coordination sites by MeCN as a result of a single-electron reduction followed by CO dissociation, which is further supported by the formation of **3** (0.9 mM), as evidenced by the post-electrolysis UV-Vis spectrum (Figure S9[†]). Upon dividing the moles of CO produced by the moles of **1** (25 μmol) for the three points located in the plateau regime, a mean value of 0.98 ± 0.05 was obtained, which approximates to unity. These findings indicate that after a single-electron reduction, complex **1** effectively generates vacant sites followed by MeCN coordination.

To further confirm electrocatalysis, we electrolyzed complex **1** (1 mM) at the second reduction peak (-1.88 V vs Fc/Fc⁺) in the presence of ¹³CO₂ in wet electrolyte. After a 3 h bulk electrolysis, the cell headspace was examined using IR spectroscopy. The gaseous sample contained both ¹³CO and ¹²CO, as shown in Figure 7a. The presence of ¹³CO confirmed the electrocatalytic conversion of CO₂ to CO. Based on the proposed mechanism (Figure 1), the presence of ¹²CO was anticipated; the mechanism involves the formation of an Mn-CO₂H moiety, and subsequent protonation followed by H₂O loss to generate [Mn(bpy)(CO)₄]⁺. In agreement with that of reported Mn-based electrocatalysts,^{35,36} the mechanism under ¹³CO₂ results in a [Mn(bpy)(¹³CO)(¹²CO)₃]⁺ intermediate, which subsequently leads to either ¹²CO or ¹³CO dissociation before regenerating the active catalyst. Therefore, one can reasonably anticipate as much as a 1:3 ratio of ¹³CO and ¹²CO in the product stream formed with **1** as a precatalyst and an on-cycle intermediate for electrocatalytic CO₂ reduction to CO (Figure 7b).

After electrolyzing 25 μmol of **1** at the second reduction potential under CO₂ for 3 h, we detected 85 μmol of CO (Figure S7b[†], black dots). Considering the CO evolution from the dissociation process in the same time period (Figure S7b[†], blue dots), ~65 μmol of CO can be associated with the catalytic conversion, yielding a turnover number of 2.4. Figures of merit were selected to compare the efficiency of **1** with that of the benchmark catalyst **2**, as shown in Table 2. The quantity (*i*_{cat}/*i*_p) obtained from CV also provides insight into the relative turnover frequencies.³⁵ Here, *i*_{cat} is the peak current under 5% H₂O in MeCN saturated with CO₂, and *i*_p is the peak current under inert conditions (dry electrolyte). The ratio of *i*_{cat} to *i*_p gives information related to the kinetics of the corresponding reaction.

Table 2. Efficiency Comparison of Complexes **1** and **2** for the Reduction of CO₂ to CO.

Complex	ϕ _{CO} ^a (%)	E _{app} ^b (V)	η ^c (V)	<i>i</i> _{cat} / <i>i</i> _p
1	80	-1.88	0.67	2.1
2	75	-1.86	0.65	1.6

^aAverage ϕ_{CO} obtained from a 3 h bulk electrolysis. ^bReferenced to Fc/Fc⁺. ^cEach overpotential was calculated from the difference between the thermodynamic redox potential and the applied potential. The formal redox potential for CO formation is -1.21 V vs. Fc/Fc⁺ in nonaqueous media.³⁷

Complex **1** shows a *i*_{cat}/*i*_p value that is slightly larger than that of complex **2**; we suspect that this is a result of the increased lability of the axial CO ligand in complex **1** as compared to the lability of the axial Br in complex **2**.

Identification of Intermediates Pertinent to CO₂ Reduction

We studied the first reductive process of **1** using IR spectroscopy. Due to the air sensitivity of the reduced species, bulk electrolysis with **1** was carried out at -1.48 V vs Fc/Fc⁺ under a nitrogen atmosphere to avoid any oxygen exposure, and the electrolyte was then transferred into a sealed transmission cell and monitored using FT-IR spectroscopy. After a 5 min bulk electrolysis, the CO bands of the pristine complex disappear and new bands corresponding to complex **3** appear, including a broad band around 1960 cm⁻¹ and a sharp band centered at 2050 cm⁻¹ (Figure 8a, grey squares). This new vibrational pattern indicating the presence of a tricarbonyl species further supports the occurrence of CO dissociation at the first reduction potential. The other new bands at 1850–1900 cm⁻¹ (with two shoulders at 1930–1970 cm⁻¹) is assigned to the formation of [Mn₂(CO)₆(bpy)₂] (Figure 8a, black circles). Based on these observations, an EC mechanism is proposed, as shown in Fig. 8b.

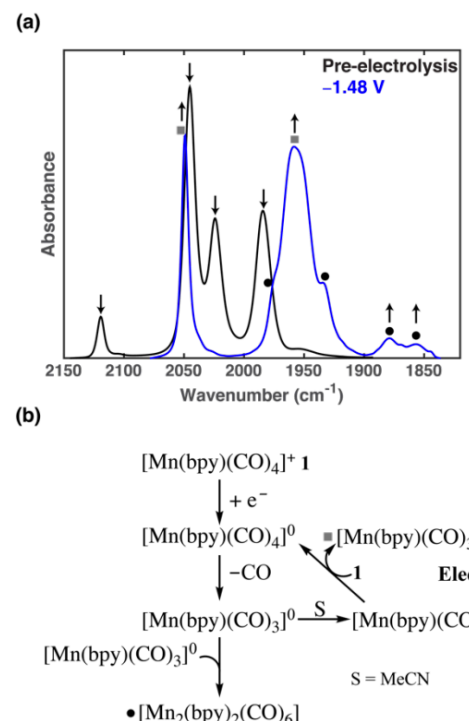


Figure 8. (a) IR spectral changes of **1** before and after a 5 minute bulk electrolysis at -1.48 V vs. Fc/Fc⁺ under Ar. The new peaks correspond to the formation of two species: complex **3** (■) and the Mn-Mn bonded dimer (●). Schematic electrochemical reaction mechanism of **1** at the first reduction potential.

However, we did not detect the presence of the singly reduced [Mn(bpy)(CO)₄]⁰, which is anticipated to be too unstable at room temperature to observe; a similar observation was also reported for the analogous Re system. As discussed in the previous section, [Mn(bpy)(CO)₄]⁰ can undergo CO dissociation to form the five-coordinate radical [Mn(bpy)(CO)₃]⁰, which is short-lived at room temperature. This radical can either dimerize or be captured by MeCN to form the solvato radical ([Mn(bpy)(CO)₃(MeCN)]⁰), which is unstable at room temperature. This solvato intermediate can transfer its electron to **1** to form **3** and [Mn(bpy)(CO)₄]⁰; the electron transfer is thermodynamically feasible since the reduction potential of **3** is slightly more negative with respect to that of **1** (Figure 4b).

Clearly, the observations of **3** and the Mn–Mn-bonded dimer provide evidence of reduction-induced CO dissociation.

Next, the second reductive process of **1** was monitored via *in situ* UV-Vis spectroscopy, and the results are shown in Figure 9. During a bulk electrolysis at -1.88 V vs Fc/Fc⁺ (conducted in a customized quartz cuvette with a Pt gauze working electrode), the band corresponding to **1** (~330 nm) decreased, with a new band growing at ~370 nm and new features at 500–800 nm (Figure 9a, inset). The former band is attributed to the formation of **3** (grey squares), whereas the new band at ~550 nm reveals the formation of the five-coordinate $[\text{Mn}(\text{bpy})(\text{CO})_3]^-$ (grey stars). This observation is consistent with the UV-Vis spectral changes of **2** at the second reduction potential (Figure S11[†]). Interestingly, both **3** and the Mn–Mn-bonded dimer (black circles) were observed during the second reductive process. In light of the proposed EC mechanism (Figure 9b), the five-coordinate radical $[\text{Mn}(\text{bpy})(\text{CO})_3]^0$ can be involved in several possible pathways in the subsequent reduction (Figure 9b); it can rapidly dimerize owing to its transient nature, and after receiving the second electron, the dimer can undergo cleavage of the Mn–Mn bond, generating the key intermediate $[\text{Mn}(\text{bpy})(\text{CO})_3]^-$ and $[\text{Mn}(\text{bpy})(\text{CO})_4]^0$. Another possibility is that $[\text{Mn}(\text{bpy})(\text{CO})_3]^0$ can be solvated by MeCN to form the solvato radical. This solvato radical can reduce **1** to yield **3** and $[\text{Mn}(\text{bpy})(\text{CO})_4]^0$ (as discussed in the previous section). In agreement with the calculation studies, the overall

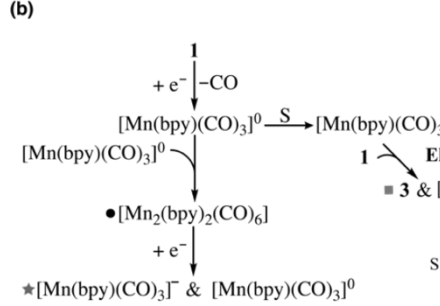
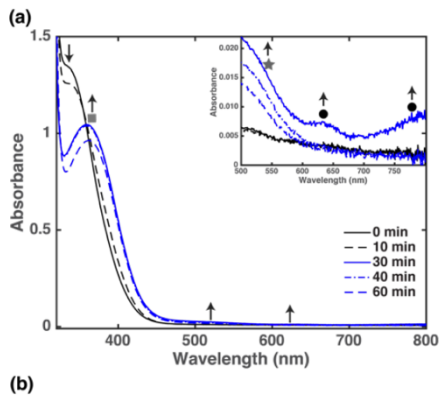


Figure 9. (a) *In situ* UV-Vis spectral changes for complex **1** at -1.88 V vs Fc/Fc⁺ under Ar. The new peaks correspond to the formation of the following species: complex **3**, $[\text{Mn}(\text{bpy})(\text{CO})_3]^-$, and the Mn–Mn-bonded dimer. (b) Schematic mechanism for the formation of $[\text{Mn}(\text{bpy})(\text{CO})_3]^-$ via **1** at the second reduction potential.

experimental results show that **1** functions as one of the intermediates and as a precatalyst in the Mn-based CO₂ catalytic cycle, as it can generate the five-coordinate anion, $[\text{Mn}(\text{bpy})(\text{CO})_3]^-$, a critical intermediate to bind and reduce CO₂.

Conclusions

We experimentally demonstrated that the tetracarbonyl cation **1** is a precatalyst and an on-cycle intermediate that can be electrochemically transformed into the active catalyst $[\text{Mn}(\text{bpy})(\text{CO})_3]^-$ for CO₂ reduction to CO in the presence of a proton source. Complex **1** has been studied using X-ray crystallography, IR and UV-Vis spectroscopy, and DFT calculations. One of the axial Mn–CO bonds exhibits a surprisingly decreased level of π back-bonding. The electrochemical properties of **1** were studied using cyclic voltammetry and compared with those of two benchmark complexes **2** and **3**. Complex **1** undergoes a reduction-induced CO dissociation and subsequent solvation in MeCN. Importantly, the formation of the active catalyst $[\text{Mn}(\text{bpy})(\text{CO})_3]^-$ via two single-electron reductions of **1**, detected using an *in situ* UV-Vis study, indicates that complex **1** is an intermediate present in the Mn-mediated CO₂ electrocatalytic system.

Experimental Section

General Procedures

All experiments were performed in the absence of light except during the weighing of solid samples. Schlenk techniques and anhydrous solvents were used for the synthesis of all complexes. All reagents (reagent grade) were obtained from commercial suppliers and used without further purification unless otherwise noted. Anhydrous MeCN and CH₂Cl₂ were purchased from Sigma-Aldrich (Sure/Seal). TBAH (Sigma-Aldrich) was dried under vacuum overnight prior to use. Manganese pentacarbonyl bromide (Strem), 2,2'-bipyridine (Sigma-Aldrich), and silver hexafluoroantimonate (Sigma-Aldrich) were used as received. Manganese complexes were carefully handled with minimal light exposure.

Electrochemical Studies

For all electrochemical experiments, the electrolyte was bubbled with the desired gas (Ar or CO₂) for 15 min prior to taking a background scan to ensure a featureless background from 0 to -2.9 V vs Fc/Fc⁺. After adding the desired complex, the electrolyte was bubbled for an additional 5 min prior to data collection. Complexes were loaded at a concentration of 1 mM for both CV and bulk electrolysis. Ferrocene was added as an internal reference. The total volume of electrolyte used for these experiments was 10 mL for CV and 25 mL for bulk electrolysis. The bulk electrolyses were operated for ~4 h, and the headspace was analyzed using GC approximately every 20 min. The proton concentration was kept consistent for the Ar and CO₂ trials using pH-adjusted water with HClO₄ and neutral water, respectively. Electrolytes were prepared by dissolving TBAH in anhydrous MeCN in a Schlenk flask. The electrolyte was stored under an inert atmosphere and purged immediately prior to use. A 3-mm-diameter glassy carbon disk electrode (BASi MF-2012) was used in all electrochemical experiments.

Potentials were first referred to an Ag/AgNO₃ (10 mM) electrode (BASi MW-1085) in 0.1 M TBAH/MeCN and then referenced to Fc/Fc⁺. A platinum mesh (~1 cm²) attached to a platinum wire was used as the counter electrode in all electrochemical measurements. A 15 mL three-neck round-bottom flask was used as the electrochemical cell for CV, and a 70 mL four-neck homemade jacketed flask was used for bulk electrolysis. The working electrode and reference electrodes were secured using “mini” Ace-threaded adaptors from Ace-glass (No. 7 and No. 8, respectively). The counter electrode was threaded through a septum, which was then fitted on to one neck of the cell.

Instrumentation

Electrochemical measurements were performed on a Model CHI 760D electrochemical workstation (CH Instruments, Austin, TX). NMR spectra were recorded on a Bruker AVANCE spectrometer (500 MHz for ¹H nuclei and 125 MHz for ¹³C nuclei). FT-IR spectra were recorded on a Nicolet Model iS50 FT-IR spectrometer for gas and liquid samples, and a Nicolet Model 6700 FT-IR spectrometer equipped with a single- reflection diamond ATR attachment for solid samples. UV-Vis spectra and photoprocesses were monitored using a Cary 60 UV-Vis spectrophotometer (Agilent Technologies). X-ray diffraction data were collected with a Bruker Photon 100 CMOS system equipped with a Mo K α μ s microfocus source ($\lambda = 0.71073$ Å). The frames were integrated with the Bruker SAINT software package using a narrow-frame algorithm. CO production was analyzed using a 70 °C isothermal method over 5 min on an HP 6890 gas chromatograph and TCD with a Molsieve 5A PLOT capillary column (Agilent) running He as the flow gas. H₂ was sampled with an SRI 8610C gas chromatograph and TCD with a Molsieve column (HAYSEP D) and Ar flow gas. A 7-min isotherm at 80 °C was employed.

Computational Methodology

Gaussian 16 via density functional theory (DFT) with the M06 functional level of theory and 6-311G** basis set were used to perform geometry optimization and frequency calculations of the ground state, singlet and doublet of the molecules of interest. To alleviate computational costs, we applied LANL2D basis set on the manganese metal center. The LANL2D basis set describes the inner electrons of the metal with effective core potentials. Additionally, a solvent continuum model with acetonitrile was utilized, since all electrochemical measurements were conducted in the presence of acetonitrile. All frequency calculations carried out on stationary points yielded zero imaginary frequencies. HOMO and LUMO energy levels were extracted from the calculations.

Syntheses

[Mn(bpy)(CO)₄][SbF₆] (1). [Mn(bpy)(CO)₃Br] (0.15 g, 0.40 mmol) and AgSbF₆ (0.21 g, 0.61 mmol) were mixed in 25 mL of anhydrous CH₂Cl₂. CO gas was bubbled through the solution in the absence of light with constant stirring at room temperature. After 40 min, the solution was filtered through a Celite pad and

the filtrate was evaporated to yield a yellow solid. Reprecipitation from CH₂Cl₂/Et₂O (1/10, 120 mL) afforded 0.070 g (40% yield) of a yellow microcrystalline solid, which was washed several times with Et₂O and dried in vacuo. IR (ATR-IR, ν_{CO} in cm⁻¹): 2116 (s), 2022 (w), 1967 (w), 1938 (sh). UV-Vis data in CH₂Cl₂ (λ_{max} in nm): 330. ¹H NMR (500 MHz, CD₂Cl₂) δ 8.93 (d, J = 5.5 Hz, 1H), 8.44 (d, J = 8.1 Hz, 1H), 8.31 (t, J = 7.9 Hz, 1H), 7.78 (t, J = 6.6 Hz, 1H). ¹³C NMR (126 MHz, CD₂Cl₂) δ 213.55, 205.02, 156.00, 154.92, 141.71, 129.08, 124.90.

[Mn(bpy)(CO)₃Br] (2). This complex was synthesized according to the literature⁵ and characterized using IR spectroscopy in MeCN (ν_{CO} in cm⁻¹): 2028 (s), 1930 (m).

[Mn(bpy)(CO)₃(MeCN)][PF₆] (3). This complex was also synthesized according to the literature.⁵ IR spectroscopy in MeCN (ν_{CO} in cm⁻¹): 2050 (s), 1958 (w). ¹H NMR (500 MHz, CD₃CN) δ 9.14 (d, J = 5.5 Hz, 1H), 8.40 (d, J = 8.1 Hz, 1H), 8.23 (td, J = 7.9, 1.5 Hz, 1H), 7.71 (dd, J = 7.6, 5.6 Hz, 1H). ¹³C NMR (126 MHz, CD₃CN) δ 218.95, 217.97, 156.50, 154.96, 140.85, 128.14, 127.90, 124.14.

Conflicts of interest

There are no conflicts to declare.

Acknowledgements

Financial support for this work was provided by the National Science Foundation under grant CHE-1800400. Any opinions, findings, and conclusions or recommendations expressed in this material are those of the authors and do not necessarily reflect the views of the National Science Foundation.

Notes and references

- White, J. L.; Baruch, M. F.; Pander, J. E.; Hu, Y.; Fortmeyer, I. C.; Park, J. E.; Zhang, T.; Liao, K.; Gu, J.; Yan, Y.; et al. Light-Driven Heterogeneous Reduction of Carbon Dioxide: Photocatalysts and Photoelectrodes. *Chem. Rev.* **2015**, *115* (23), 12888–12935.
- Grills, D. C.; Ertem, M. Z.; McKinnon, M.; Ngo, K. T.; Rochford, J. Mechanistic Aspects of CO₂ Reduction Catalysis with Manganese-Based Molecular Catalysts. *Coord. Chem. Rev.* **2018**, *374*, 173–217.
- Elgrishi, N.; Chambers, M. B.; Wang, X.; Fontecave, M. Molecular Polypyridine-Based Metal Complexes as Catalysts for the Reduction of CO₂. *Chem. Soc. Rev.* **2017**, *46* (3), 761–796.
- Grice, K. A. Carbon Dioxide Reduction with Homogenous Early Transition Metal Complexes: Opportunities and Challenges for Developing CO₂ Catalysis. *Coord. Chem. Rev.* **2017**, *336*, 78–95.
- Costentin, C.; Robert, M.; Savéant, J.-M. Catalysis of the Electrochemical Reduction of Carbon Dioxide. *Chem. Soc. Rev.* **2013**, *42* (6), 2423–2436.

<https://doi.org/10.1039/C2CS35360A>.

(6) Stanbury, M.; Compain, J.-D.; Chardon-Noblat, S. Electro and Photoreduction of CO₂ Driven by Manganese-Carbonyl Molecular Catalysts. *Coord. Chem. Rev.* **2018**, *361*, 120–137.

(7) Hawecker, J.; Lehn, J.-M.; Ziessel, R. Electrocatalytic Reduction of Carbon Dioxide Mediated by Re(Bipy)(CO)₃Cl (Bipy = 2,2'-Bipyridine). *J. Chem. Soc. Chem. Commun.* **1984**, No. 6, 328–330.

(8) Takeda, H.; Cometto, C.; Ishitani, O.; Robert, M. Electrons, Photons, Protons and Earth-Abundant Metal Complexes for Molecular Catalysis of CO₂ Reduction. *ACS Catal.* **2017**, *7* (1), 70–88.

(9) Sinopoli, A.; La Porte, N. T.; Martinez, J. F.; Wasielewski, M. R.; Sohail, M. Manganese Carbonyl Complexes for CO₂ Reduction. *Coord. Chem. Rev.* **2018**, *365*, 60–74.

(10) Bourrez, M.; Molton, F.; Chardon-Noblat, S.; Deronzier, A. [Mn(Bipyridyl)(CO)₃Br]: An Abundant Metal Carbonyl Complex as Efficient Electrocatalyst for CO₂ Reduction. *Angew. Chem. Int. Ed.* **2011**, *50* (42), 9903–9906.

(11) Francke, R.; Schille, B.; Roemelt, M. Homogeneously Catalyzed Electroreduction of Carbon Dioxide—Methods, Mechanisms, and Catalysts. *Chem. Rev.* **2018**, *118* (9), 4631–4701.

(12) Graves, C.; Ebbesen, S. D.; Mogensen, M.; Lackner, K. S. Sustainable Hydrocarbon Fuels by Recycling CO₂ and H₂O with Renewable or Nuclear Energy. *Renew. Sustain. Energy Rev.* **2011**, *15* (1), 1–23.

(13) Smieja, J. M.; Sampson, M. D.; Grice, K. A.; Benson, E. E.; Froehlich, J. D.; Kubiak, C. P. Manganese as a Substitute for Rhenium in CO₂ Reduction Catalysts: The Importance of Acids. *Inorg. Chem.* **2013**, *52* (5), 2484–2491.

(14) Grills, D. C.; Farrington, J. A.; Layne, B. H.; Lymar, S. V.; Mello, B. A.; Preses, J. M.; Wishart, J. F. Mechanism of the Formation of a Mn-Based CO₂ Reduction Catalyst Revealed by Pulse Radiolysis with Time-Resolved Infrared Detection. *J. Am. Chem. Soc.* **2014**, *136* (15), 5563–5566.

(15) Bourrez, M.; Orio, M.; Molton, F.; Vezin, H.; Duboc, C.; Deronzier, A.; Chardon-Noblat, S. Pulsed-EPR Evidence of a Manganese(II) Hydroxycarbonyl Intermediate in the Electrocatalytic Reduction of Carbon Dioxide by a Manganese Bipyridyl Derivative. *Angew. Chem. Int. Ed.* **2014**, *53* (1), 240–243.

(16) Riplinger, C.; Carter, E. A. Influence of Weak Brønsted Acids on Electrocatalytic CO₂ Reduction by Manganese and Rhenium Bipyridine Catalysts. *ACS Catal.* **2015**, *5* (2), 900–908.

(17) Riplinger, C.; Sampson, M. D.; Ritzmann, A. M.; Kubiak, C. P.; Carter, E. A. Mechanistic Contrasts between Manganese and Rhenium Bipyridine Electrocatalysts for the Reduction of Carbon Dioxide. *J. Am. Chem. Soc.* **2014**, *136* (46), 16285–16298.

(18) Grice, K. A.; Gu, N. X.; Sampson, M. D.; Kubiak, C. P. Carbon Monoxide Release Catalysed by Electron Transfer: Electrochemical and Spectroscopic Investigations of [Re(Bpy-R)(CO)₄](OTf) Complexes Relevant to CO₂ Reduction. *Dalton Trans.* **2013**, *42* (23), 8498–8503.

(19) Shaver, R. J.; Rillema, D. P. Physical and Photophysical Properties of Rhenium(I) Tetracarbonyl Complexes. *Inorg. Chem.* **1992**, *31* (20), 4101–4107.

(20) S. P. Schmidt, J. Nitschke, W. C. Trogler, S. I. Huckett and R. J. Angelici, in *Inorganic Syntheses*, John Wiley & Sons, Ltd, 2007, pp. 113–117

(21) Yempally, V.; Kyran, S. J.; Raju, R. K.; Fan, W. Y.; Brothers, E. N.; Darenbourg, D. J.; Bengali, A. A. Thermal and Photochemical Reactivity of Manganese Tricarbonyl and Tetracarbonyl Complexes with a Bulky Diazabutadiene Ligand. *Inorg. Chem.* **2014**, *53* (8), 4081–4088.

(22) Beck, W.; Suenkel, K. Metal Complexes of Weakly Coordinating Anions. Precursors of Strong Cationic Organometallic Lewis Acids. *Chem. Rev.* **1988**, *88* (7), 1405–1421.

(23) Agarwal, J.; iii, C. J. S.; Shaw, T. W.; Vandezande, J. E.; Majetich, G. F.; Bocarsly, A. B.; iii, H. F. S. Exploring the Effect of Axial Ligand Substitution (X = Br, NCS, CN) on the Photodecomposition and Electrochemical Activity of [MnX(N–C)(CO)₃] Complexes. *Dalton Trans.* **2015**, *44* (5), 2122–2131.

(24) Pereira, C.; Ferreira, H. G.; Schultz, M. S.; Milanez, J.; Izidoro, M.; Leme, P. C.; Santos, R. H. A.; Gambardella, M. T. P.; Castellano, E. E.; Lima-Neto, B. S.; et al. Probing the Electronic Factors Responsible for the Cyclic Electron-Transfer Induced Isomerism Fac \rightleftharpoons mer: Synthesis, Electrochemical and Spectroscopic Studies of Fac-[Mn(CO)₃(L'–L')]¹⁰⁺ Complexes. *Inorganica Chim. Acta* **2005**, *358* (13), 3735–3744.

(25) Ault, B. S.; Becker, T. M.; Li, G. Q.; Orchin, M. The Infrared Spectra and Theoretical Calculations of Frequencies of Fac-Tricarbonyl Octahedral Complexes of Manganese(I). *Spectrochim. Acta. A. Mol. Biomol. Spectrosc.* **2004**, *60* (11), 2567–2572.

(26) Hutchinson, B.; Nakamoto, K. Infrared Spectra of Group VIB Metal Carbonyls Containing Heterocyclic Diamines. *Inorganica Chim. Acta* **1969**, *3*, 591–595.

(27) Scheiring, T.; Kaim, W.; Fiedler, J. Geometrical and Electronic Structures of the Acetyl Complex Re(Bpy)(CO)₃(COCH₃) and of [M(Bpy)(CO)₄](OTf), M=Mn, Re. *J. Organomet. Chem.* **2000**, *598* (1), 136–141.

(28) Carriero, G. A.; Pérez-Martínez, J. A.; Miguel, D.; Riera, V.; García-Granda, S.; Pérez-Carreño, E. The Reduction and Oxidation of Cationic Carbonyl Complexes of Manganese with Phosphoniodithioformate: X-Ray Crystal Structure of [Mn(CO)₄(S₂CPCy₃)][ClO₄]. *J. Organomet. Chem.* **1996**, *511* (1), 77–84.

(29) Tignor, S. E.; Kuo, H.-Y.; Lee, T. S.; Scholes, G. D.; Bocarsly, A. B. Manganese-Based Catalysts with Varying Ligand Substituents for the Electrochemical Reduction of CO₂ to CO. *Organometallics* **2019**, *38* (6), 1292–1299.

(30) Kuo, H.-Y.; Lee, T. S.; Chu, A. T.; Tignor, S. E.; Scholes, G. D.; Bocarsly, A. B. A Cyanide-Bridged Di-Manganese Carbonyl Complex That Photochemically Reduces CO₂ to CO. *Dalton Trans.* **2019**, *48* (4), 1226–1236.

(31) Clark, M. L.; Grice, K. A.; Moore, C. E.; Rheingold, A. L.; Kubiak, C. P. Electrocatalytic CO₂ Reduction by M(Bpy-R)(CO)₄ (M = Mo, W; R = H, TBu) Complexes. Electrochemical, Spectroscopic, and Computational Studies and Comparison with Group 7 Catalysts. *Chem. Sci.* **2014**, *5* (5), 1894–1900.

(32) Tory, J.; Setterfield-Price, B.; Dryfe, R. A. W.; Hartl, F. [M(CO)₄(2,2'-Bipyridine)] (M=Cr, Mo, W) Complexes as Efficient Catalysts for Electrochemical Reduction of CO₂ at a Gold Electrode. *ChemElectroChem* **2015**, *2* (2), 213–217.

(33) Machan, C. W.; Sampson, M. D.; Chabolla, S. A.; Dang, T.; Kubiak, C. P. Developing a Mechanistic Understanding of Molecular Electrocatalysts for CO₂ Reduction Using Infrared

Spectroelectrochemistry. *Organometallics* **2014**, *33* (18), 4550–4559.

(34) Hartl, F.; Rossenaar, B. D.; Stor, G. J.; Stufkens, D. J. Role of an Electron-Transfer Chain Reaction in the Unusual Photochemical Formation of Five-Coordinated Anions $[\text{Mn}(\text{CO})_3(\alpha\text{-Diimine})]^-$ from $\text{Fac-}[\text{Mn}(\text{X})(\text{CO})_3(\alpha\text{-Diimine})]$ ($\text{X} = \text{Halide}$) at Low Temperatures. *Recl. Trav. Chim. Pays-Bas* **1995**, *114* (11–12), 565–570.

(35) Agarwal, J.; Shaw, T. W.; Schaefer, H. F.; Bocarsly, A. B. Design of a Catalytic Active Site for Electrochemical CO_2 Reduction with $\text{Mn}(\text{I})$ -Tricarbonyl Species. *Inorg. Chem.* **2015**, *54* (11), 5285–5294.

(36) Agarwal, J.; Shaw, T. W.; Stanton, C. J.; Majetich, G. F.; Bocarsly, A. B.; Schaefer, H. F. NHC-Containing Manganese(I) Electrocatalysts for the Two-Electron Reduction of CO_2 . *Angew. Chem. Int. Ed.* **2014**, *53* (20), 5152–5155.

(37) Costentin, C.; Drouet, S.; Robert, M.; Savéant, J.-M. A Local Proton Source Enhances CO_2 Electroreduction to CO by a Molecular Fe Catalyst. *Science* **2012**, *338* (6103), 90–94.